Collimated fast electron beam generation in critical density plasma

T. Iwawaki, H. Habara, S. Baton, K. Morita, J. Fuchs, S. Chen, M. Nakatsutsumi, C. Rousseaux, F. Filippi, W. Nazarov, and K. A. Tanaka

Citation: Physics of Plasmas (1994-present) **21**, 113103 (2014); doi: 10.1063/1.4900868
View online: http://dx.doi.org/10.1063/1.4900868
View Table of Contents: http://scitation.aip.org/content/aip/journal/pop/21/11?ver=pdfcov
Published by the AIP Publishing

Collimated fast electron beam generation in critical density plasma

T. Iwawaki,[1,a)] H. Habara,[1] S. Baton,[2] K. Morita,[1] J. Fuchs,[2] S. Chen,[2] M. Nakatsutsumi,[2,3] C. Rousseaux,[4] F. Filippi,[5] W. Nazarov,[6] and K. A. Tanaka[1]
[1]*Graduate School of Engineering, Osaka University, 2-1, Yamada-oka, Suita, Osaka 565-0871, Japan*
[2]*LULI, CNRS-Ecole Polytechnique-Université Pierre et Marie Curie-CEA, 91128 Palaiseau, France*
[3]*European X-Ray Free-Electron Laser Facility (XFEL) GmbH, Germany*
[4]*CEA, DAM, DIF, F-91297 Arpajon, France*
[5]*La SAPIENZA, University of Rome, Dip. SBAI, 00161 Rome, Italy*
[6]*School of Chemistry, University of St. Andrews, North Haugh, St. Andrews, Fife KY16 9ST, Scotland, United Kingdom*

(Received 4 July 2014; accepted 14 October 2014; published online 7 November 2014)

Significantly collimated fast electron beam with a divergence angle 10° (FWHM) is observed when an ultra-intense laser pulse ($I = 10^{14}$ W/cm^2, 300 fs) irradiates a uniform critical density plasma. The uniform plasma is created through the ionization of an ultra-low density (5 mg/c.c.) plastic foam by X-ray burst from the interaction of intense laser ($I = 10^{14}$ W/cm^2, 600 ps) with a thin Cu foil. 2D Particle-In-Cell (PIC) simulation well reproduces the collimated electron beam with a strong magnetic field in the region of the laser pulse propagation. To understand the physical mechanism of the collimation, we calculate energetic electron motion in the magnetic field obtained from the 2D PIC simulation. As the results, the strong magnetic field (300 MG) collimates electrons with energy over a few MeV. This collimation mechanism may attract attention in many applications such as electron acceleration, electron microscope and fast ignition of laser fusion. © *2014 AIP Publishing LLC*.
[http://dx.doi.org/10.1063/1.4900868]

I. INTRODUCTION

In the frame of the fast ignition (FI) scheme of inertial confinement fusion,[1] several methods have been proposed to heat the core plasma by an external source.[2] Direct heating method (super-penetration) is one such method owing to the simple target and laser geometry.[3] In this scheme, ultra-intense laser pulse (UILP) irradiates an imploded plasma directly and propagates into the corona region with relativistic self-focusing (RSF). When the UILP reaches critical density surface, relativistic induced transparency (RIT) allows the pulse to propagate as a single channel up to critical[4] or 10 times critical density.[5] In the end, the laser energy is transferred to electrons at the critical or overcritical density interface.[5] In our previous work, the emission divergence of fast electron beam has been found significantly narrower (33°(FWHM)) than that obtained at the plain foil target (66°(FWHM)) when the UILP penetrated into several tens μm overdense plasma.[6] However, the understanding of physical mechanism has been left as an issue.

This motivated us to investigate the characteristics of the fast electron generated around critical density plasmas in detail in well characterized experimental platform. For this purpose, we create homogeneous critical density plasma inside a small capillary tube filled with ultra low-density plastic foam. The foam is heated by X-ray burst produced by irradiating a thin Cu foil with an ns infrared laser pulse. The plasma density profile is estimated by a 1D hydro-radiative simulation as well as 2D X-ray radiography measurement that show creation of homogeneous critical density plasma over several hundred microns inside the tube.[7] When an UILP (10^{19} W/cm^2) irradiates the plasma, energetic electron beam is created via $J \times B$ heating, B-loop acceleration, and betatron resonance acceleration.[8–10] The spatial distribution of the generated electron beam emitted from the tube toward the laser direction is observed with an imaging plate (IP) stack. The beam divergence of fast electrons is $11 \pm 2°$ (FWHM), i.e., around a quarter of the one ($45 \pm 6°$ (FWHM)) measured in the case of the standard foil target. This significant narrow divergence is also observed in 2D Particle-In-Cell (PIC) simulation. To understand the physical mechanism of the collimation, we calculated the motion of electrons that follows Lorentz force using magnetic field obtained from 2D PIC calculation. It is found that the structure of magnetic field associated with the laser propagation in critical density plasma strongly collimates strongly fast electrons that with energy over a few MeV.

II. PRODUCTION OF ULTRA-LOW DENSITY FOAMS

In-situ polymerisation is a method of moulding foams to desired shape and inside hollow metallic or plastic components of laser targets. Production of ultra-low density foams inside targets eliminates handling of fragile low density foams. The diameter and depth of the targets, the aspect ratio, and also the design of the target is crucial and predominantly dictates the methods used for their synthesis. The formation of in-situ foams in laser targets involves filling and polymerisation step; depending on the target aspect ratio, the correct acrylate monomer/mixture of monomers are dissolved in a suitable solvent and using a micro needle injected inside the target cavity. The solution is then illuminated with correct wavelength of UV light appropriate to the monomers utilized. The solution inside the target cavity gels

[a)]iwawaki-t@eie.eng.osaka-u.ac.jp

within seconds and targets containing the wet gel are then transferred to correct solvent for exchange. Finally the target containing the wet foam is transferred to a critical point dryer, and using liquid CO_2 as critical solvent the wet gels are dried. As a consequence of these steps, some components of the targets are fixed after the foam filling process to minimize the damage to the final target.

III. EXPERIMENTAL RESULT

The experiment was performed at the ELFIE facility at LULI, École Polytechnique using two laser beams. The experimental setup is shown in Fig. 1. The target consists of polyimide tube, ultra-low density foam and thin Cu foil. The wall thickness, the length, and the inside diameter of the polyimide tube are 20 μm, 300 μm, and 254 μm, respectively. The plastic ($C_{15}H_{20}O_6$) foam is filled in the tube with the ultra-low density of 5 mg/cc that corresponds to the critical density of 10^{21}/cc when the foam is ionized. The thin Cu foil (0.7 μm thick) is attached to one side of the tube for production of X-ray burst to ionize the foam material.[7] X-rays are created by irradiation of the Cu foil with an infrared ($\lambda = 1.057$ μm) laser pulse (60 J/600 ps) at focused intensity of 10^{14} W/cm^2. The plasma density and temperature have been estimated by the 1D hydro-radiative simulation, CHIC.[11] In addition, we have measured the density of the solid and ionized foam by performing 2D X-ray radiography. The source was a burst of Kα X-rays produced by irradiating a 20 μm glass wire with a high intensity short pulse laser. The spectrum of X-rays was predominantly Kα X-rays from non-ionized silicon atoms at 1.74 keV; this was confirmed using step filters and post-processing of the data. The X-ray absorption in the cold foam matched the transmission properties as tabulated in CXRO.[12] As for the ionized foam in the temperature range that we were expecting (20–40 eV), the transmission data showed that the electron density of the ionized foam was 10^{21}/c.c. 600–800 ps after irradiation of the heating beam. Since the nano structures of the foam may disappear after the time (=10 ps) given by the ratio of the nano scale divided by the sound speed, the plasma within the tube should be rather uniform at this timing. This analysis was performed with the aid of the code FLYCHK.[13] This X- ray absorption technique is rather insensitive to the range of temperatures of 10–40 eV, whereas the transmission depends more on the electron density, hence we are convinced that the desired density was achieved in the heating process.[14]

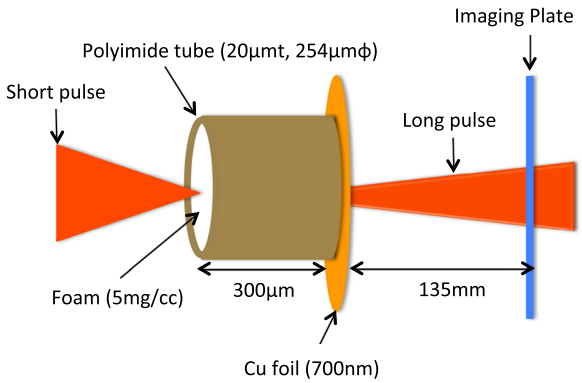

FIG. 1. Experimental setup. A long (600 ps) pulse laser irradiates a thin Cu foil (0.7 μm) to generate X-ray burst that ionizes the entire foam target to create uniform critical density plasma. An UILP comes from the left side for producing a plasma channel in the plasma.

The UILP is then focused on the surface of the critical density plasma from the open side of the tube (from the left in Fig. 1) after the foam becomes the expected density. The laser wavelength is 1.057 μm with 300 fs time duration. The laser is focused with an $f/3$ off-axis parabola to a 10 μm diameter spot producing an intensity of 10^{19} W/cm^2 in vacuum. The pointing accuracy is at least one tenth or smaller than the diameter of the entire foam plasma. The emission pattern of electron beam from the target is detected by a SR IP set at 135 mm behind the target.[15,16] This IP is covered with a 7 μm thick Al foil to protect the IP from laser light. Electrons with energies over 25 keV can be detected through the Al foil based on the continuous-slowing-down approximation (CSDA) range calculation.[17] A thin Al foil target is also used for comparison. The Al target is 20 μm thick with 1 mm $\times$ 1 mm square. Through the experiment, the short pulse is kept at normal incidence. Typical experimental results of electron beam divergence on IP are shown in Fig. 2. Figs. 2(a) and 2(b) indicate the fast electron divergence for the Al foil and the tube target, respectively. The black circle and line in each figure correspond to the entrance of the long pulse beam to the target and the entrance to a detector (not presented in the paper), respectively. In order to observe the electron beam as emitted from the target but avoiding the overlap with the black circle, the tube target was tilted in the horizontal plane with respect to the short and long pulse beam axis by 7°. It is clearly shown that the electron beam from the tube target is significantly collimated compared to that obtained from the Al foil target. Green solid lines in Figs. 2(c) and 2(d) indicate line profiles of the green lines in Figs. 2(a) and 2(b), respectively. Red dashed lines in Figs. 2(c) and 2(d) show the results of fitting the line profile (green solid line) using Gaussian fitting. Considering the fitting results and the experiment setup, the divergence angle from the foil target is 45° $\pm$ 6° (FWHM), consistent with past studies.[6,18,19] On the other hand, the angle from the tube target is only 11° $\pm$ 2° (FWHM), around quarter in comparison to the foil target case.

Although IP is sensitive also to X-rays and protons, fast electron signal is predominantly recorded in these patterns. As to the signal in the foil target, there is a uniform background ($\sim$1000 PSL). This may come from X-rays. The proton divergence was separately measured to be 35° (FWHM) for 1.7 MeV and is narrower than the observed divergence. Thus, the signal in Fig. 2(a) is considered to be fast electrons. As to the signal in the tube target, the contribution from X-rays should be smaller than the foil due to the low target Z number ($Z = 3.7$) and can be neglected. Protons are mainly accelerated in the radial direction based on the PIC in Ref. 10. Our PIC simulation (the details are given in Sec. IV) indicates also similar large divergence and the signal intensity on the IP from protons could be 20 times smaller than that from electrons.[16,20,21] Thus, the narrow divergence signal is due to fast electrons.

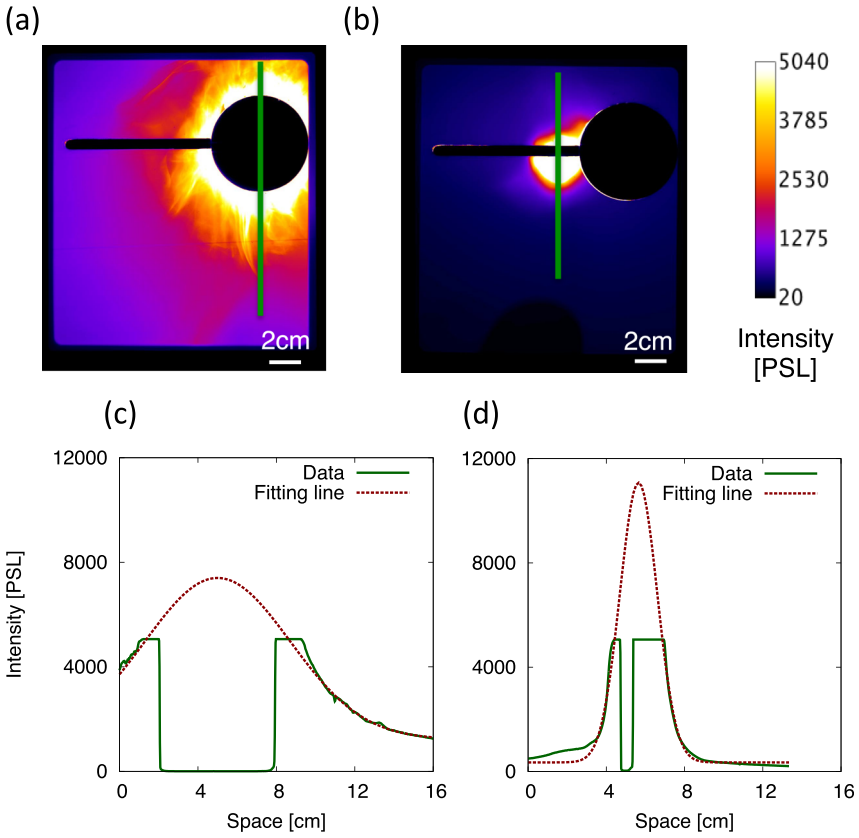

FIG. 2. Typical results of electron beam divergence observed on IP stack from 135 mm behind the target. (a) Al foil target case. The electron divergence is $45° \pm 6°$ (FWHM). (b) Tube target case. The electron divergence is $11° \pm 2°$(FWHM). (c) Green solid line shows line profile of the green line in (a). Red dashed line shows fitting profile using Gaussian shape. (d) Green solid line shows line profile of the green line in (b). Red dashed line shows fitting profile using Gaussian shape.

IV. PIC SIMULATION

In order to understand the experimental results, we conducted 2D PIC simulations (FISCOF (Refs. 22–25)) using the experimental configurations. The electron density of the tube target is set to be the critical density. The vertical size and the thickness of the critical density plasma are 140 μm and 60 μm, respectively. The target thickness is shorter than the actual target due to the calculation capacity. Since the laser channeling is observed in this simulation up to 40 μm in depth, this simulation setup can model the experiment. Preformed plasma is also attached on the surface and the density exponentially decays to 0.1 N_c with the scale length of 2 μm referring to the CHIC calculation. This preformed plasma is necessary to represent the plasma expansion due to the X-rays flash created by the long pulse laser beam. On the other hand, the electron density of the foil target is set to be 10 N_c. This electron density is lower than the actual target due to the calculation capacity. Though the relativistic critical density ($\gamma N_c = 3.4\ N_c$) is lower than the target density, this simulation setup can model the interaction in the overdense plasma. The vertical size and the thickness of the plasma are 70 μm and 1 μm, respectively. Preformed plasma is also attached with a 1 μm scale length from 5.0 to 0.1 N_c. The temporal distribution of the incident laser intensity is a Gaussian with 300 fs (FWHM) pulse duration. The maximum intensity is set to be 3×10^{19} W/cm^2 with the spot size of 10 μm. The pulse is injected at 5 μm in front of the foot of preformed plasma. Fast electrons are observed at 10 μm from rear surface of the plasmas. Figure 3(a) shows the angular distributions of fast electrons (>25 keV) for both plasma cases from the simulation. The red solid and green dotted lines indicate the cases of the critical density plasma and the foil, respectively. Fast electrons from the critical density plasma have a small divergence angle of 12° (FWHM) from laser axis. Within this angle, 48% of the total fast electron energy is confined. Comparatively, the electron beam from the foil target shows a large divergence of an angle 25° (FWHM). There is some difference on the divergence angle of the foil between the experiment and PIC. This difference could be due to the scale length of the preplasma used in the PIC (1 μm).[26,27] Longer preplasma will produce electrons with a larger divergence due to Weibel instability growth. Figure 3(b) shows the electron energy spectra for both target cases from the simulation. The red solid and green dotted lines also indicate the cases of the critical density plasma and the foil, respectively. Here, we note that the most electrons carried energies of over 1 MeV, namely, 90% for the critical density plasma and 83% for the foil.

In this simulation, we observed also protons created in the critical density plasma. The cut off energy, average energy and divergence angle are 5 MeV, 0.5 MeV, and 138° (FWHM), respectively. Assuming the conversion efficiency from laser to proton energy of 1% and using proton sensitivity for IP,[20,21] signal intensity on the IP from protons are 20 times smaller than that from electrons.[16]

V. POST PROCESS ANALYSIS

Since 2D PIC simulation results reproduce the observation in the experiments qualitatively, we proceed further to find the predominant mechanism for electron collimation. When the UILP interacts with matters or plasmas, strong electrostatic or magnetic field can be generated. Especially

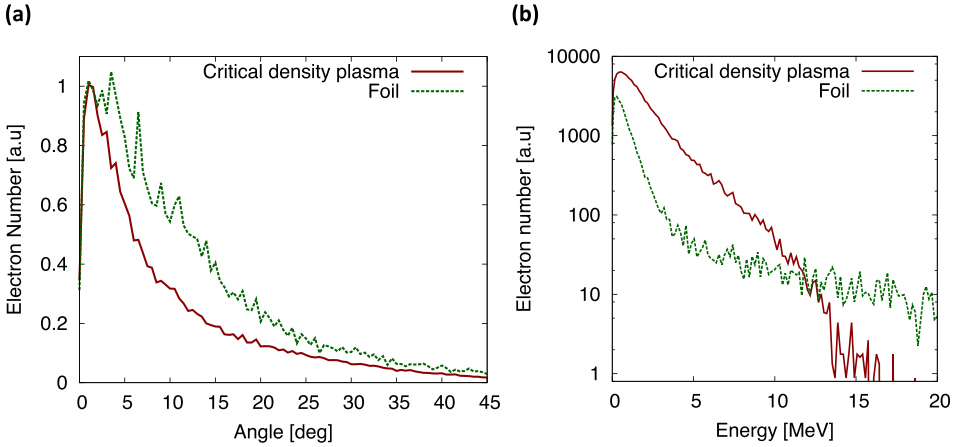

FIG. 3. Electron beam divergences (a) and spectra (b) that detected at the observation line separated 10 μm from the target rear surface in PIC simulation. The red solid line corresponds to the critical density plasma case and the green dotted line to the foil target case.

the magnetic field is known to function as an electron collimator[28–30] or scatterer.[26,27] Here, we explain the collimation mechanism as the result of the magnetic field.

A. Foil target

Figure 4(a) shows typical magnetic field structure taken at the timing of 600 fs as calculated by the PIC code in Sec. IV. Here, the maximum laser intensity reaches the critical density surface at 400 fs. The laser pulse propagates from the left toward x direction. The initial plasma location is $5\ \mu\text{m} < x < 6\ \mu\text{m}$ and $-35\ \mu\text{m} < y < 35\ \mu\text{m}$ with density of 10 N_c. The surface magnetic fields become enhanced through the positive feedback loop by surface propagation of fast electrons.[31] The strength of the fields on the target front surface reaches 400 MG and is higher than the one at behind the target.

Here, we introduce test electrons to understand how the magnetic field affects on the electron collimation using a uniform incident angular distribution as shown by the green solid line in Fig. 4(b). The motions of the electrons in this magnetic field are calculated using Lorentz force, $\mathbf{F} = -e(\mathbf{v} \times \mathbf{B})$. Initial source position of the test electrons is set at the critical surface with 10 μm diameter taking into account of laser spot size. The tracks of 5 MeV electrons are shown by white lines in Fig. 4(a). Most of electrons are reflected by the surface magnetic field to the backward and only a few electrons can pass through the target. Direction angles of the electrons are recorded when the electron passes the simulation boundaries as shown in Fig. 4(b) for the different electron energies. The electron numbers in each angle are normalized by the numbers of the input distribution. When the electron energy is 5 MeV (blue dashed lines in Fig. 4(b)), the electron numbers in $-20° \sim 20°$ is not so different from the input. However, the number drops for $-100° \sim -50°$ and $50° \sim 100°$, and increases for $-180° \sim -100°$ and $100° \sim 180°$. These trends are same also as 10 MeV electrons (red solid lines). Those electrons merge into the surface current that reinforce the strength of surface magnetic field as a positive feedback. On the other hand, in the case of 10 MeV electrons, forward electrons observed between $-20°$ and $20°$ seem to increase because the electron energy is high enough to break through the surface magnetic field. In addition, electron motion is concentrated to the forward by the rear magnetic field.

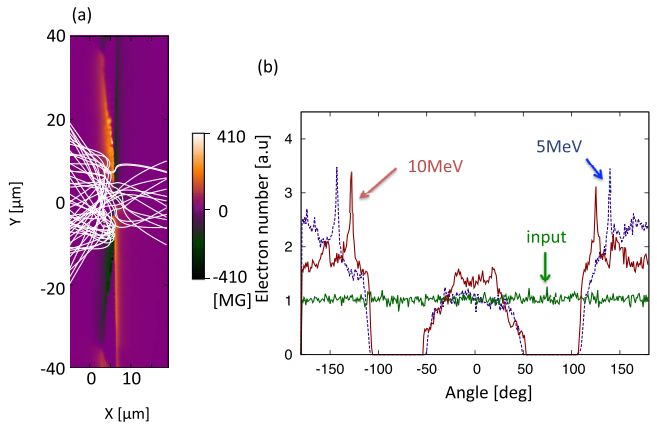

FIG. 4. (a) Typical structure (orange and back) of magnetic field induced by electron beam at 600 fs. The strength reaches as high as 400 MGauss. Electrons (5 MeV) are guided by the magnetic field (white lines). (b) Electron angular distribution detected at simulation boundaries. The horizontal axis is angle from the laser axis and the vertical axis is electron number. Green line indicates the input distribution. Blue and red lines show the distribution of electrons for energies 5 MeV and 10 MeV.

Here, we introduce the parameter "Enhancement factor (EF)" to estimate this collimation effect. This value is defined as the maximum electron normalized by the input electron numbers between $-45°$ and $45°$. Namely, the magnetic field works as a collimator when this value >1 and a reflector when <1. EF for 10 MeV electrons is 1.5 in Fig. 4(b) compared to no increase for 5 MeV electrons. Thus, the collimation effect becomes significant for higher energy electrons. Figure 5 shows relation of EFs and magnetic field strength as a function of time. Red, blue, and green solid lines in Fig. 5 indicate the time development of the EFs for 0.5, 5, and 10 MeV electron energies, respectively. While each EF peaks at around 200–300 fs, the magnetic field strength peaks at 500 fs. Comparing these three solid lines, the collimation effect works until 300 fs especially to low energy electrons. However, the effect becomes weak after 300 fs especially for low energy electron with the development of magnetic field as shown black dashed line. Namely, after 300 fs, the collimation effect works only for high energy electrons ($\sim$10 MeV). The strong magnetic field

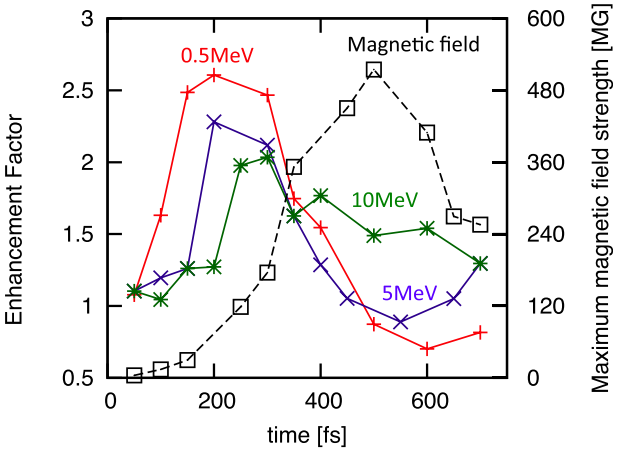

FIG. 5. Time evolution of "EF" and surface magnetic field for Al solid foil target. Red, blue, and green solid lines indicate the EFs for electron energies 0.5, 5, and 10 MeV, respectively. Black dashed line expresses the magnetic field strength. At the early time until 300 fs, every EF is larger than 1. After 300 fs, EFs decrease and become less than 1 at 600 fs except for the 10 MeV. The maximum laser intensity reaches the critical density surface at 400 fs.

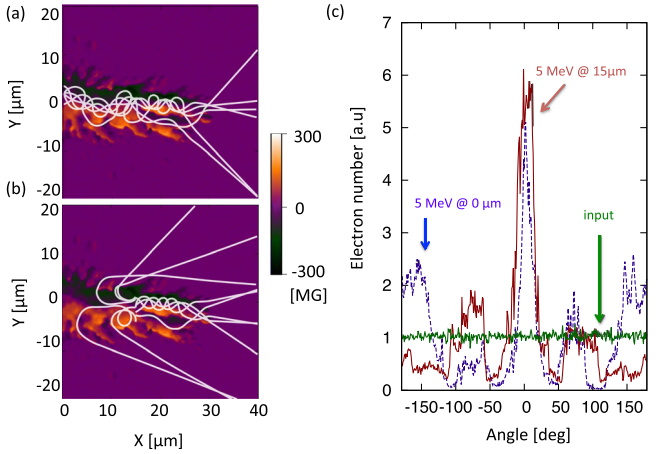

FIG. 6. Typical magnetic field generated in the critical density plasma at 600 fs and 5 MeV electron tracks (white lines) are shown for source position $x = 0\ \mu$m (a) and $x = 15\ \mu$m (b). The maximum strength is 300 MG and the vertical length is about 10 μm that corresponds to the laser spot size. It is found that for $x = 0\ \mu$m, electrons are bound and propagate along the field, while for $x = 15\ \mu$m, backward electrons are pulled into forward direction. When these electrons arrive at the simulation boundaries, the angles from laser axis are encoded. (c) The angular distribution of fast electrons 5 MeV. These source positions are $x = 0\ \mu$m (blue dashed) and $x = 15\ \mu$m (red solid), respectively. The green solid line indicates the input distribution. Comparing these two lines, it is found that the components in $-180^\circ \sim -130^\circ$ and $130^\circ \sim 180^\circ$ region merge into smaller angular regions. The peak value becomes also higher at $x = 15\ \mu$m compared $x = 0\ \mu$m.

starts working as a reflector for low energy electron. The reason may be explained using the Larmor radius represented as $r_L = m_e c^2 \sqrt{\gamma^2 - 1}/(eB)$. Here, m_e and γ are the electron mass and the electron Lorenz factor. The radius becomes small when the magnetic field is strong and the electron energy is low. Here, the radiuses of 0.5 and 10 MeV electron in 300 MG magnetic field are 0.1 and 1.1 μm, respectively. Therefore, if the electron energy is high enough, the electron breaks through the strong magnetic field region without crucial modification of the propagation direction. This post process analysis and PIC calculation in Fig. 3(b) support the large divergence of fast electrons for the case of foil target.

B. Critical density plasma

Next, electron motion in critical density plasma is calculated by using the laser conditions same as the foil target. Figure 6(a) shows typical structure of the magnetic field taken at the timing of 600 fs calculated by PIC simulations in Sec. IV. The initial plasma location is $0\ \mu\text{m} < x < 60\ \mu\text{m}$ and $-70\ \mu\text{m} < y < 70\ \mu\text{m}$ with density of N_c. Here, the maximum laser intensity reaches the critical density surface at 400 fs. This field is created by fast electron current propagating into the plasma from the left to the right in the figure. The magnetic field is located in the region of the plasma channel. The return currents can cover the boundary and neutralize the outside magnetic field.[32]

Tracks of 5 MeV electrons are shown as white lines in Fig. 6(a). The input electron source position is set at $x = 0\ \mu$m corresponding to entrance of the critical density plasma and at the y-axis same as the foil case. It is found that a number of electrons are bound around the field and propagate to forward direction rather different from the foil target case. The UILP penetrates inside the critical density plasma due to relativistic effect. The observed penetrated length is 40 μm. Therefore, the electron source is not a point localized at the entrance but rather is elongated along the plasma channel. Then, we consider different source position, for example, center of magnetic fields ($x = 15\ \mu$m). Figure 6(b) represents the same magnetic field as Fig. 6(a). White lines in Fig. 6(b) show the tracks of 5 MeV electrons assuming the source position at $x = 15\ \mu$m. In the results, backward electrons are pulled into the forward direction. A portion of these electrons is also bound around the field and propagates to the forward. Others escape from the field before arriving at the end of the magnetic field. These trends can be also seen in Fig. 6(c), which represents the angular distribution in the two cases corresponding to Figs. 6(a) and 6(b). The green solid line shows the input source. The blue dashed line corresponds to the case $x = 0\ \mu$m, and the red solid one to the case $x = 15\ \mu$m. One can see that the forward current increases significantly and the backward current is smaller than that in the foil target. Backward electrons ($-180^\circ < \Theta < -130^\circ$ or $130^\circ < \Theta < 180^\circ$) increase to a level twice the input when the source position is set at the entrance of the field. However, in the case of middle source position, the backward peaks shift to smaller angles ($-100^\circ < \Theta < -50^\circ$ or $50^\circ < \Theta < 100^\circ$) where the electrons can easily escape from the field. In addition, the forward electrons slightly increase.

Figure 7 shows the temporal evolution of forward electrons for different electron energies and magnetic fields. The blue and purple solid lines indicate the EFs of 0.5 and 5 MeV electron from the source at $x = 0\ \mu$m, respectively. In addition, the electron energy at $x = 15\ \mu$m is also shown by the red dotted line. Until 400 fs, each EFs exceed 1 and the lower energy (0.5 MeV) electrons appear to have a higher EF. On the contrary after 400 fs, the higher energy electrons have higher EF. EF of low energy electrons decreases to less

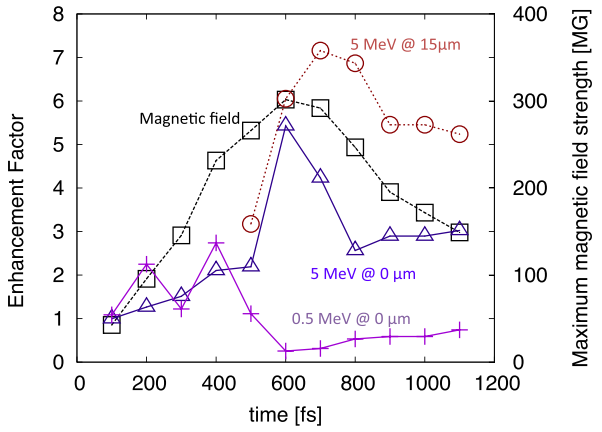

FIG. 7. Time dependence of EFs and the maximum strength of magnetic field in the plasma. The purple and blue solid lines indicate the EFs with the source at $x = 0\ \mu$m for 0.5 and 5 MeV, respectively. The red dotted line also indicates EFs for the source set at $x = 15\ \mu$m and the energy at 5 MeV. The tendency of low energy electron represented by the purple line is same as Fig. 5. The 5 MeV electron shown by the blue line indicates high collimation effect especially at 600 fs. When the source position is set at $x = 15\ \mu$m, the collimation effect works more efficiently. Black dashed line expresses the magnetic field strength. The maximum laser intensity reaches the critical density surface at 400 fs.

than 1 after 600 fs, whereas the EF of high energy electron is kept higher than 1. In case of critical density plasma, it is easy even for low energy electrons to enter the target because the surface magnetic field is weak (~10 MG). Once the electrons enter the target, these electrons are trapped immediately by the magnetic field generated in the plasma channel. The maximum magnetic field in the plasma channel (black dashed line in Fig. 7) reaches hundreds of MG resulting in the Larmor radius less than 1 μm and smaller than the size of magnetic field. In our estimation, 11% of the 0.5 MeV electrons are trapped in the field at 600 fs. In addition, even if the electrons are bound around the field, it is difficult to propagate along the field but rather escape at large angle. On the other hand, if the energy is high enough, the electron are bound around the field and propagate in forward direction with a good collimation even if the source position is $x = 0\ \mu$m (blue lines in Figs. 6(c) and 7). In fact, this effect becomes more prominent when the source is embedded in the field (red dotted line in Figs. 6(c) and 7). From the above observation, the magnetic field in the critical density plasma works as a collimator for the electrons that have energy over a few MeV.

Due to the sheath potential at the rear side of the target, electrons under the average energy or lower than the temperature ($T_e = 2.3$ MeV in Fig. 3(b)) may be trapped within the target.[15,23] Therefore, the observed collimated fast electrons in Fig. 2(b) are mainly the ones with energy larger than the average energy (in the plasma) collimated through the magnetic field and escaped from the tube target.

VI. DISCUSSION

So far we have shown that the electron beam divergence is strongly related to both structure and strength of the magnetic fields and electron energy. For the foil target, the surface magnetic field plays a dominant role on electron divergence. For the critical density plasma, the surface field becomes minor compared to the field inside the plasma channel. This magnetic field inside the channel makes electron collimation. Here, we assume the main part of electron beam is generated after the peak intensity reaches the target (after 400 fs). Then, in the foil target case, it can be assumed that high energy electron (~10 MeV) can pass through the surface magnetic field easily and the collimation effect becomes effective as shown in Fig. 5. In the critical density plasma, the collimation effect becomes effective for over a few MeV electrons. The collimation in critical density plasma works much better than that in the foil target as shown in Figs. 5 and 7. These trends are also explained by PIC simulations as shown in Fig. 8. Figure 8 shows the total electron energy observed in the simulation at the observation line indicating the electron flux in the forward direction for (a) the foil target and (b) the critical density plasma, respectively. The energy is divided into five bands: <0.5, 0.5 ~ 2.0, 2.0 ~ 5.0, 5.0 ~ 10.0, and >10.0 MeV. In the case of foil target, only higher energy electrons tend to reach the observation line especially after 500 fs, while, in case of the critical density plasma, it is clear that even lower energy electrons can pass

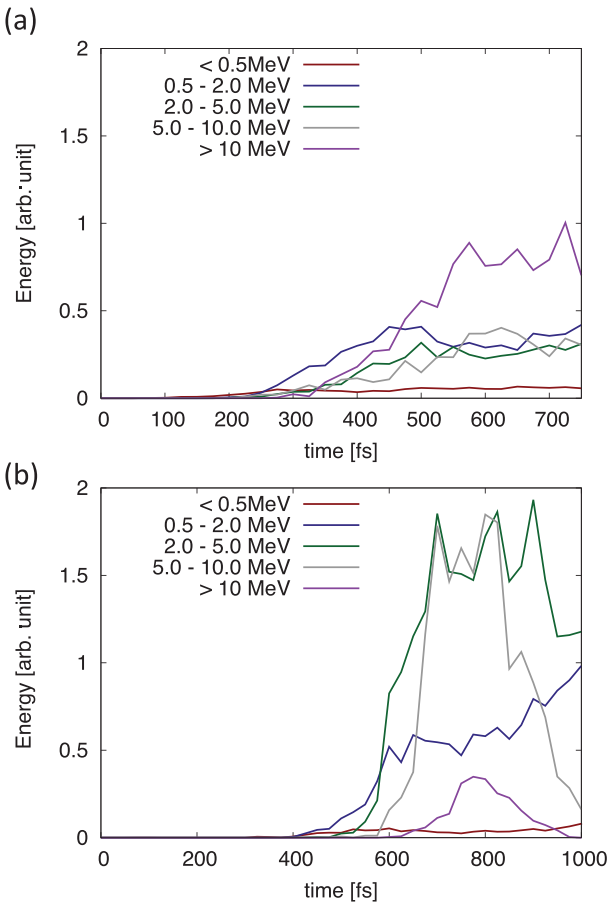

FIG. 8. Energy of electrons that pass through the observation line (forward direction) within per unit time. Red, blue, green, gray, and purple lines indicate different electron energy bands at <0.5, 0.5 ~ 2.0, 2.0 ~ 5.0, 5.0 ~ 10.0, and >10.0 MeV, respectively. The foil target case is shown by (a) and the critical density plasma case is shown by (b). In the foil target, only high energy electrons can pass through the target. On the other hand, in the critical density plasma, over a few MeV electrons can be bound and propagate along the magnetic field region.

through the line. The flux is more than several times this one obtained in foil target. These results can also explain the difference of the electron beam behavior.

Based on the results given so far, it is possible to consider a case for the fast electron collimation in further over-dense plasmas. When the magnetic field in plasma channel is created by the forward going electrons, same argument can be applied in the over-dense region as the one in the critical density plasma, represented as $B(r) = (2\pi/c)en_e v_e r$. Here, n_e, v_e, and r are background electron density, electron speed, and radius of the plasma channel, respectively. In case of this critical density plasma, the maximum strength of the magnetic field was 300 MG. Using the channel radius 5 μm and the background electron density N_c, the electron speed in the channel is estimated to be 0.18 c. Assuming the same speed when the UILP with the wavelength 1 μm penetrates 10 times critical density plasma with the diffraction limit ($r = 0.5\ \mu$m), the maximum strength of the magnetic field is also estimated to be 300 MG. This strong magnetic field could collimate significantly the fast electron beam.

VII. CONCLUSION

Significantly collimated fast electron beam (>25 keV) has been observed from the uniform and long critical density plasma irradiated with an ultra-intense laser pulse at 10^{19} W/cm^2. The divergence was 11° (FWHM), much smaller than that the 45° from the standard foil target. 2D PIC simulations for the two types of target indicated the same trend. Based on our post process analysis using magnetic fields taken from the 2D PIC simulations, it is possible to explain the experiment by considering the both structure and strength of the magnetic field. Therefore, we conclude that the difference of the electron beam divergence is caused by the difference of the structure and strength of the magnetic field in the two targets. Similar magnetic field collimation has been observed in guiding cone wire target,[28] target surface,[31] resistivity controlled solid target[29] and preformed magnetic field structure.[30] However, a difference in our case is that strong magnetic fields are used for the collimation along the plasma channel in a critical and/or over-critical density. In addition, the generated electron beam has higher density and lower averaged energy compared to those from the wake field acceleration[33,34] and the surface waves acceleration[35,36] where relatively low density plasma is used. There may be an attractive application of this collimation and high intensity electron beam over a few MeV electrons to the direct heating of high density core such as super-penetration mode in fast ignition.[32,37]

ACKNOWLEDGMENTS

The authors gratefully acknowledge the support of the staff of the ELFIE in the execution of this work (11-TW-F4). Moreover, we thank Professor H. Sakagami at National Institute for Fusion Science for his permission of use of 2D-PIC FISCOF code and Dr. P. Nicolai at Université Bordeaux for conducting 1D CHIC hydro-radiative simulation. A part of this work was supported by Grants-in-Aid for Scientific Research, type *A* (Grant No. 22246122) and type *B* (Grant No. 23360412) and JSPS Research Fellowship for young scientists (25 · 858), Cooperation toward Leadership in Innovative Creation (CLIC) Internship Program and X-ray free electron laser priority strategy program of MEXT (12005014 Osaka University).

[1]M. Tabak, J. Hammer, M. E. Glinsky, W. L. Kruer, S. C. Wilks, J. Woodworth, E. Michael Campbell, M. D. Perry, and R. J. Mason, Phys. Plasmas **1**, 1626 (1994).
[2]R. Kodama, K. Mima, K. A. Tanaka, Y. Kitagawa, H. Fujita, K. Takahashi, A. Sunahara, K. Fujita, H. Habara, T. Jitsuno, Y. Sentoku, T. Matsushita, T. Miyakoshi, N. Miyanaga, T. Norimatsu, H. Setoguchi, T. Sonomoto, M. Tanpo, Y. Toyama, and T. Yamanaka, Phys. Plasmas **8**, 2268 (2001).
[3]K. A. Tanaka, R. Kodama, H. Fujita, M. Heya, N. Izumi, Y. Kato, Y. Kitagawa, K. Mima, N. Miyanaga, T. Norimatsu, A. Pukhov, A. Sunahara, K. Takahashi, M. Allen, H. Habara, T. Iwatani, T. Matusita, T. Miyakosi, M. Mori, H. Setoguchi, T. Sonomoto, M. Tanpo, S. Tohyama, H. Azuma, T. Kawasaki, T. Komeno, O. Maekawa, S. Matsuo, T. Shozaki, K. Suzuki, H. Yoshida, and T. Yamanaka, Phys. Plasmas **7**, 2014 (2000); K. A. Tanaka, M. M. Allen, A. Pukhov, R. Kodama, H. Fujita, Y. Kato, T. Kawasaki, Y. Kitagawa, K. Mima, N. Morio, H. Shiraga, M. Iwata, T. Miyakoshi, and T. Yamanaka, Phys. Rev. E **62**, 2672 (2000); K. A. Tanaka, R. Kodama, Y. Kitagawa, K. Kondo, K. Mima, H. Azechi, Z. Chen, S. Fujioka, H. Fujita, T. Johzaki, A. Lei, T. Matsuoka, K. Mima, N. Miyanaga, K. Nagai, H. Nagatomo, H. Nishimura, T. Norimatsu, K. Shigemori, H. Shiraga, M. Tanpo, Y. Tohyama, T. Yabuuchi, J. Zheng, Y. Izawa, P. A. Norreys, R. Stephens, and S. Hatchett, Plasma Phys. Controlled Fusion **46**, B41–B49 (2004).
[4]S. Ivancic, W. Theobald, D. Haberberger, D. H. Froula, K. S. Anderson, D. D. Meyerhofer, K. Tanaka, H. Habara, and T. Iwawaki, in Proceedings of the 55th Annual Meeting of the APS Division of Plasma Physics, Denver, CO, 11–15 November 2013.
[5]A. L. Lei, A. Pukhov, R. Kodama, T. Yabuuchi, K. Adumi, K. Endo, R. R. Freeman, H. Habara, Y. Kitagawa, K. Kondo, G. R. Kumar, T. Matsuoka, K. Mima, H. Nagatomo, T. Norimatsu, O. Shorokhov, R. Snavely, X. Q. Yang, J. Zheng, and K. A. Tanaka, Phys. Rev. E **76**, 066403 (2007).
[6]T. Tanimoto, A. L. Lei, T. Yabuuchi, H. Habara, K. Kondo, R. Kodama, K. Mima, and K. A. Tanaka, J. Phys.: Conf. Ser. **112**, 022095 (2008).
[7]R. J. Mason, R. A. Kopp, H. X. Vu, D. C. Wilson, S. R. Goldman *et al.*, Phys. Plasmas **5**, 211 (1998).
[8]W. L. Kruer and K. Estabrook, Phys. Fluid **28**, 430 (1985).
[9]A. Pukhov and J. Meyer-ter-Vehn, Phys. Plasma **5**, 1880 (1998).
[10]A. Pukhov, Z.-M. Sheng, and J. Meyer-ter-Vehn, Phys. Plasma **6**, 2847 (1999).
[11]P. H. Maire, R. Abgrall, J. Breil, and J. Ovadia, SIAM J. Sci. Comput. **29**, 1781 (2007).
[12]B. L. Henke, E. M. Gullikson, and J. C. Davis, At. Data Nucl. Data Tables **54**, 181–342 (1993).
[13]H.-K. Chung, M. H. Chen, W. L. Morgan, Y. Ralchenko, and R. W. Lee, High Energy Density Phys. **1**, 3–12 (2005).
[14]S. Chen, F. Filippi, J. Fuchs, S. Baton, M. Nakatsutsumi, C. Rousseaux, T. Iwawaki, K. Morita, H. Habara, and K. A. Tanaka, "Density controlled plasma creation using ultra-low density plastic foam," Phys. Plasmas (unpublished).
[15]T. Yabuuchi, K. Adumi, H. Habara, R. Kodama, K. Kondo, T. Tanimoto, K. A. Tanaka, Y. Sentoku, T. Matsuoka, Z. L. Chen, M. Tampo, A. L. Lei, and K. Mima, Phys. Plasma **14**, 040706 (2007).
[16]K. A. Tanaka, T. Yabuuchi, T. Sato, R. Kodama, Y. Kitagawa, T. Takahashi, T. Ikeda, Y. Honda, and S. Okuda, Rev. Sci. Instrum. **76**, 013507 (2005).
[17]See http://physics.nist.gov/PhysRefData/Star/Text/ESTAR.html for ESTAR—National Institute of Standards and Technology, Physical Meas. Laboratory.
[18]J. S. Green, V. M. Ovchinnikov, R. G. Evans, K. U. Akli, H. Azechi, F. N. Beg, C. Bellei, R. R. Freeman, H. Habara, R. Heathcote, M. H. Key, J. A. King, K. L. Lancaster, N. C. Lopes, T. Ma, A. J. MacKinnon, K. Markey, A. McPhee, Z. Najmudin, P. Nilson, R. Onofrei, R. Stephens, K. Takeda, K. A. Tanaka, W. Theobald, T. Tanimoto, J. Waugh, L. Van Woerkom, N. C. Woolsey, M. Zepf, J. R. Davies, and P. A. Norreys, Phys. Rev. Lett. **100**, 015003 (2008).
[19]Y. T. Li, J. Zhang, Z. M. Sheng, J. Zheng, Z. L. Chen, R. Kodama, T. Matsuoka, M. Tampo, K. A. Tanaka, T. Tsutsumi, and T. Yabuuchi, Phys. Rev. E **69**, 036405 (2004).
[20]T. Bonnet, M. Comet, D. Denis-Petit, F. Gobet, F. Hannachi, M. Tarisien, M. Versteegen, and M. M. Aleonard, Rev. Sci. Instrum. **84**, 013508 (2013).

[21]J. F. Ziegler, Transport of Ions in matter (TRIM), See http://www.srim.org.
[22]H. Sakagami and K. Mima, in *Proceedings of the 2nd International Conference on Inertial Fusion Sciences and Applications, Kyoto, 2001* (Elsevier, 2002), pp. 380–383.
[23]H. Habara, K. Ohta, K. A. Tanaka, G. R. Kumar, M. Krishnamurthy, S. Kahaly, S. Mondal, M. K. Bhuyan, R. Rajeev, and J. Zheng, Phys. Rev. Lett. **104**, 055001 (2010).
[24]S. Inoue, S. Tokita, K. Otani, M. Hashida, M. Hata, H. Sakagami, T. Taguchi, and S. Sakabe, Phys. Rev. Lett. **109**, 185001 (2012).
[25]Y. Uematsu, S. Ivancic, T. Iwawaki, H. Habara, A. L. Lei, W. Theobald, and K. A. Tanaka, Rev. Sci. Instrum. **85**, 11E612 (2014).
[26]A. Debayle, J. J. Honrubia, E. d'Humières, and V. T. Tikhonchuk, Phys. Rev. E **82**, 036405 (2010).
[27]V. M. Ovchinnikov, D. W. Schumacher, M. McMahon, E. A. Chowdhury, C. D. Chen, A. Morace, and R. R. Freeman, Phys. Rev. Lett **110**, 065007 (2013).
[28]R. Kodama, Y. Sentoku, Z. L. Chen, G. R. Kumar, S. P. Hatchett, Y. Toyama, T. E. Cowan, R. R. Freeman, J. Fuchs, Y. Izawa, M. H. Key, Y. Kitagawa, K. Kondo, T. Matsuoka, H. Nakamura, M. Nakatsutsumi, P. A. Norreys, T. Norimatsu, R. A. Snavely, R. B. Stephens, M. Tampo, K. A. Tanaka, and T. Yabuuchi, Nature **432**, 1005–1008 (2004).
[29]S. Kar, A. P. L. Robinson, D. C. Carroll, O. Lundh, K. Markey, P. McKenna, P. Norreys, and M. Zepf, Phys. Rev. Lett. **102**, 055001 (2009).
[30]R. H. H. Scott, C. Beaucourt, H.-P. Schlenvoigt, K. Markey, K. L. Lancaster, C. P. Ridgers, C. M. Brenner, J. Pasley, R. J. Gray, I. O. Musgrave, A. P. L. Robinson, K. Li, M. M. Notley, J. R. Davies, S. D. Baton, J. J. Santos, J.-L. Feugeas, Ph. Nicolai, G. Malka, V. T. Tikhonchuk, P. McKenna, D. Neely, S. J. Rose, and P. A. Norreys, Phys. Rev. Lett. **109**, 015001 (2012).
[31]H. Habara, K. Adumi, T. Yabuuchi, T. Nakamura, Z. L. Chen, M. Kashihara, R. Kodama, K. Kondo, G. R. Kumar, L. A. Lei, T. Matsuoka, K. Mima, and K. A. Tanaka, Phys. Rev. Lett. **97**, 095004 (2006).
[32]A. Pukhov and J. Meyer-ter-Vehn, Phys. Rev. Lett. **76**, 3975 (1996).
[33]T. Tajima and J. M. Dawson, Phys. Rev. Lett. **43**, 267 (1979).
[34]N. Nakanii, K. Kondo, Y. Kuramitsu, Y. Mori, E. Miura, K. Tsuji, K. Kimura, S. Fukumochi, M. Kashihara, T. Tanimoto, H. Nakamura, T. Ishikura, K. Takeda, M. Tampo, H. Takabe, R. Kodama, Y. Kitagawa, K. Mima, and K. A. Tanaka, Appl. Phys. Lett. **93**, 081501 (2008).
[35]N. Naseri, S. G. Bochkarev, and W. Rozmus, Phys. Plasmas **17**, 033107 (2010).
[36]L. Willingale, P. M. Nilson, A. G. R. Thomas, J. Cobble, R. S. Craxton, A. Maksimchuk, P. A. Norreys, T. C. Sangster, R. H. H. Scott, C. Stoeckl, C. Zulick, and K. Krushelnick, Phys. Rev. Lett. **106**, 105002 (2011).
[37]T. Matsuoka, A. Lei, T. Yabuuchi, K. Adumi, J. Zheng, R. Kodama, K. Sawai, K. Suzuki, Y. Kitagawa, T. Norimatsu, K. Nagai, H. Nagatomo, Y. Izawa, K. Mima, Y. Sentoku, and K. A. Tanaka, Plasma Phys. Controlled Fusion **50**, 105011 (2008).